This full text paper was peer reviewed at the direction of IEEE Communications Society subject matter experts for publication in the ICC 2008 proceedings.

A Comprehensive Evaluation of Joint Range and Angle Estimation in Ultra-Wideband Location Systems for Indoors

Camillo Gentile, A. Judson Braga, and Alfred Kik
National Institute of Standards and Technology
Wireless Communication Technologies Group
Gaithersburg, Maryland, USA

***Abstract*— Fine time resolution enables Ultra-Wideband (UWB) ranging systems to reliably extract the first multipath arrival corresponding to the range between a transmitter and receiver, even when attenuated in strength compared to later arrivals. Bearing systems alone lack any notion of time and in general select the arrival coinciding with the strongest path, which is rarely the first one in non line-of-sight conditions. Complementing UWB ranging systems with bearing capabilities allows indexing the arrivals as a function of both time and angle to isolate the first, providing precision range and angle. In order to gauge the limits of the joint UWB system, we carry out close to 20000 measurements up to 45 m in non line-of-sight conditions in four separate buildings with dominant wall material varying from sheet rock to steel. In addition, we report performance for varying bandwidth and center frequency of the system.**

***Index Terms*— Uniform circular array, frequency-invariant beamforming, spatial-temporal channel modeling**

I. Introduction

Location systems with ranging capabilities alone necessitate at least three base stations with knows locations to extract the two-dimensional position of an unknown device through triangulation [1]. In emergency operations such as fire rescue, no such infrastructure exists to date as part of the building code, nor does time permit installation as a crisis unravels. However if both the range and angle of the device were known, then a single base station alone could extract its location. Moreover if the base station itself were a mobile device attached to a fireman, then the system could be used to find a trapped victim equipped with a beacon tag, yielding his or her location with respect to the fireman as he moves about.

Fine time resolution and the presence of lower frequencies in the baseband to penetrate walls enable Ultra-Wideband (UWB) ranging systems to reliably extract the first multipath arrival corresponding to the range between a transmitter and receiver, even when attenuated in strength compared to later arrivals. Bearing systems alone lack any notion of time and in general select the arrival coinciding with the strongest path, which is rarely the first one in non line-of-sight conditions. Complementing UWB ranging systems with bearing capabilities allows indexing the arrivals as a function of both time and angle to isolate the first, providing precision range and angle.

Irahhauten provides a comprehensive overview of the Ultra-Wideband channel propagation measurements taken in recent years to model the *temporal* properties of the indoor channel [2], however to our knowledge only Scholtz [3] and Keignart [4] report the statistical properties of the time-of-flight besides us: a comprehensive measurement campaign in our previous work [5] shows that UWB technology can deliver precision from a few centimeters to a tens of centimeters based on the operating conditions. Suprisingly there has been very little effort to model the *spatial* properties of the UWB channel [6], [7], [8], [9], [10], but even these papers lack statistics on the angle of the first arrival, of particular interest in location systems. Analogous to our comprehensive evaluation of the time-of-flight for UWB ranging, we extend the measurement suite to include angle-of-flight as well, and show its performance according to variation in system parameters. Specifically, the main contribution of this paper is a study of the relationship between angle and range errors and their joint location error and:

- *bandwidth*: precision increases with bandwidth, but carries diminishing returns with the additional expense;
- *center frequency*: lower frequencies penetrate materials better, but higher frequencies offer better angular resolution;
- *construction material*: compare performance with typical building construction materials varying as sheet rock (easy), plaster, cinder block, to steel (most difficult) to gauge lower and upper bounds on the technology, rather than with building layout (i.e. office, residential typically have the same wall materials);
- *long range*: the high dynamic range of our system allows us to span 45 m and examine the limits in the technology inherent to the interaction with up to 10 walls.

The paper reads as follows: Section II introduces the temporal indoor channel propagation model and describes our Ultra-Wideband system to measure its properties. Incorporating a uniform circular array into the system in Section III enables characterizing the joint spatial-temporal properties of the channel from which the time and angle-of-flight can be extracted, as explained in Section IV. Section V provides the details of our equipment setup and Section VI outlines our suite of measurements, presenting results both through statistical metrics and in graphical format, followed by conclusions in the last section.

II. The temporal indoor propagation channel

The traditional model for the indoor propagation channel is an *impulse response* composed from K multipath arrivals indexed through k [11]

$$h(t) = \sum_{k=0}^{K-1} \alpha_k \delta(t - \tau_k), \tag{1}$$

where τ_k denotes the delay of the arrival in propagating between the transmitter and the receiver, and α_k denotes the complex-valued amplitude which accounts for both attenuation and phase change due to reflection, diffraction, and other specular effects introduced by walls (and other objects) on its path. Ranging systems based on *time-of-flight* estimate the delay τ_f associated with the arrival of the first impulse in the response, or *leading edge*. Since the signal propagates at the speed of light c in free space, the estimated range between the radios is $c \cdot \tau_f$.

The impulse response of the channel in (1) has a *frequency response*

$$H(f) = \sum_{k=0}^{K-1} \alpha_k e^{-j2\pi f \tau_k}, \tag{2}$$

suggesting that the channel can be characterized using *frequency diversity*: we compute $H(f) = \frac{Y(f)}{X(f)}$ by transmitting tones $X(f)$ with unit amplitude and zero phase across the channel at discrete values of f and then measuring $Y(f)$ at the receiver. Characterizing the channel in the frequency domain offers an important advantage over transmitting a fixed pulse in the time domain and recording the impulse response directly: once we sweep the 2-8 GHz band of interest, a sub-band with bandwidth B and the center frequency f_c can be selected a posteriori in varying the parameters of the system. The discrete frequency spectrum $X(f)$ translates to the time domain as the periodic sinc pulse $x(t)$ with revolution $\frac{1}{\Delta f}$ modulated at f_c [18]. The bandwidth controls the width of the pulse defined through the first zero-crossing at $\tau = \frac{1}{B}$, and in turn controls the multipath resolution of the system. Choosing Δf = 1.25 MHz allows for a maximum multipath spread of 800 ns, which proves sufficient throughout all four buildings for the arrivals to subside within one period and avoid time aliasing. The corresponding impulse response can be recovered through the Inverse Discrete Fourier Transform (IDFT)

$$h(t) = \sum_{l=0}^{\frac{B}{\Delta f}} H(f) e^{j2\pi f t} \tag{3}$$

where $f = f_c - \frac{B}{2} + l \cdot \Delta f$.

III. The Uniform Circular Array

Replacing the single antenna at the receiver with an antenna array introduces *spatial diversity* into the system. This enables measuring both the temporal and spatial properties of the UWB channel, in particular the azimuth *angle-of-flight* ϕ_f at which the leading edge hits the array at τ_f. For this purpose, we chose to implement the uniform circular array (UCA) over the uniform linear array (ULA) in light of the following two important advantages: 1) the azimuth of the UCA covers 360° in contrast to the 180° of the ULA; 2) the beam pattern of the UCA is uniform around the azimuth angle while that of the ULA broadens as the beam is steered from the boresight.

Consider the diagram in Fig. 1 for a single antenna transmitter and a uniform circular array receiver. The P elements of the UCA are arranged uniformly around its perimeter of

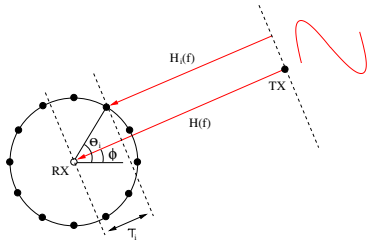

Fig. 1. The uniform circular array antenna.

radius r, each at angle $\theta_i = \frac{2\pi i}{P}$, $i = 0 \ldots P-1$. The radius determines the half-power antenna aperture corresponding to $29.2° \frac{c}{r \cdot f}$ [12]. Let $H(f)$ be the frequency response of the channel between the transmitter and reference center of the receiver array. A signal arriving from angle ϕ reaches element i with a delay $\tau_i = -\frac{r}{c}\cos(\phi + \theta_i)$ with respect to the center [13], hence the frequency response of each element is a phase-shifted version of $H(f)$, or

$$H_i(f) = H(f)e^{-j2\pi f \tau_i} = H(f)e^{j2\pi f \frac{r}{c}\cos(\phi+\theta_i)}. \tag{4}$$

In conventional beamforming, the *array frequency response* $H(f, \theta)$ is generated by shifting the phase of each element frequency response $H_i(f)$ into alignment at the reference [13]:

$$H(f,\theta) = \frac{1}{P}\sum_{i=0}^{P-1} H_i(f) e^{-j2\pi f \frac{r}{c}\cos(\theta+\theta_i)} \tag{5}$$

A peak occurs in the beam pattern for $\theta = \phi$, however the frequency-dependent phase shift in turn generates sidelobes which vary according to the frequency of operation. Fig. 2(a) illustrates the different beam patterns of the array response for f = 2 GHz and f = 8 GHz.

A. Frequency-invariant beamforming

In narrowband systems, numerous filtering techniques [13], [14], [15] exist to shape the beam pattern of the array frequency response by applying complex weights to the terms in (5). In wideband systems such as ours, these techniques could be employed, but would require designing separate filters for each sub-band; even so, it would be difficult to achieve the same beam pattern across the whole band with a finite number of elements. *Frequency-invariant beamformers* can achieve a set beam pattern over a wide frequency band of operation. The class of filters have existed over a decade for uniform linear arrays, but have recently been adapted to uniform circular arrays. They have found application primarily in directional filtering and angle-of-flight estimation [16], but to our knowledge we are the first to employ them in joint time and angle-of-flight estimation.

The development of the frequency-invariant beamformer for the uniform circular array hinges on the expansion

$$e^{j\beta\cos\gamma} = \sum_{n=-\infty}^{\infty} j^n J_n(\beta) e^{jn\gamma}, \tag{6}$$

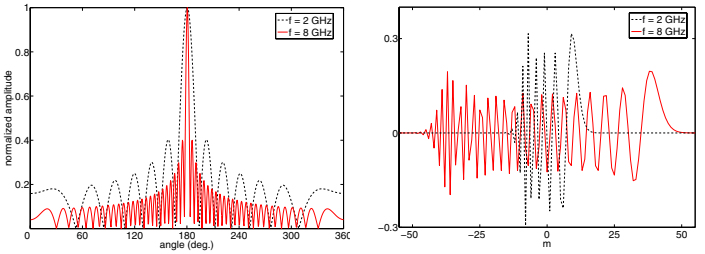

(a) The conventional beamformer. (b) The Bessel functions.

Fig. 2. The array frequency response at different frequencies.

which when applied to (4) enables separating the phase of the element frequency response into frequency-dependent and independent components:

$$H_i(f) = H(f) \sum_{n=-\infty}^{\infty} j^n J_n(2\pi f \frac{r}{c}) e^{jn(\phi+\theta_i)} \tag{7}$$

The angle ϕ can then be extracting from the above expression by introducing basis functions $e^{-jm\theta_i}$ known as *phase modes* (or modes) as in the sequel:

$$\begin{aligned}
(a)\ \hat{H}_m(f) &= \frac{1}{P}\sum_{i=0}^{P-1} H_i(f)\cdot G_m(f) e^{-jm\theta_i} \\
(b) &= H(f)\sum_{n=-\infty}^{\infty} j^n J_n(2\pi f\frac{r}{c}) e^{jn\phi}\cdot G_m(f)\left[\frac{1}{P}\sum_{i=0}^{P-1} e^{j(n-m)\frac{2\pi i}{P}}\right] \\
(c) &\approx H(f)\cdot j^m J_m(2\pi f\frac{r}{c}) e^{jm\phi}\cdot G_m(f) \\
(d) &\approx H(f)\cdot e^{jm\phi}
\end{aligned} \tag{8}$$

Transform the element frequency response into the *mode frequency response* $\hat{H}_m(f)$ in (8a) by multiplying each $H_i(f)$ by the m^{th}-mode weighted by $G_m(f)$. Substitute (7) into the expression and rearrange as in (8b). Note that the bracketed term equals 1 for $n = m + P\cdot z,\ z \in \mathcal{Z}$ and 0 otherwise, limiting the values of n in the sum. From [16], the Bessel function has the following property

$$\left|J_{|n|}(2\pi f\frac{r}{c})\right| \le \left(\frac{2\pi f\frac{r}{c}e}{2|n|}\right)^{|n|}, \tag{9}$$

so there exists a number of elements P sufficiently large such that $\left|J_{|n|}(2\pi f\frac{r}{c})\right| \approx 0$ for $|n| > \frac{P-1}{2}$; but the latter condition is always met except for $z = 0$, so the Bessel function in turn is approximately zero except for $n = m$, limiting further the values of n and simplifying (8b) to (8c). By selecting $G_m(f) = 1/j^m J_m(2\pi f\frac{r}{c})$, the expression for the mode frequency response simplifies further to (8d).

The Vandermonde structure [17] of the mode frequency response in (8d) in terms of m makes it amenable to the IDFT as a means to recover the frequency-invariant array impulse response by transforming $\hat{H}_m(f)$ from the mode domain to the angle domain $\hat{H}(f,\theta)$:

$$\hat{H}(f,\theta) = \sum_{m=-\frac{P-1}{2}}^{\frac{P-1}{2}} \hat{H}_m(f) e^{jm\theta} = H(f)\cdot \sum_{m=-\frac{P-1}{2}}^{\frac{P-1}{2}} e^{jm(\phi+\theta)} \tag{10}$$

As explained previously, $|J_{|m|}(2\pi f\frac{r}{c})| \approx 0$ (and in turn $G_m(f)$ in (8c) approaches ∞) for $|m| > \frac{P-1}{2}$, so we include only P modes in the Fourier sum above to avoid numerical instability. Fig. 2(b) displays the Bessel functions for f = 2 GHz and f = 8 GHz. Note from (9) that higher frequencies necessitate a larger number of elements P since the Bessel functions approach zero slower as m increases. So in our application the upper frequency f = 8 GHz in the band of operation determines the smallest value of P = 97 which meets the approximation for r = 24 cm.

IV. The Spatial-Temporal Indoor Propagation Channel

The *array impulse response* $h(t,\theta)$ models the spatial-temporal indoor propagation channel. It is simply the impulse response $h(t)$ in (1) augmented to characterize each multipath k not only by the delay τ_k and the complex-amplitude α_k, by also by the arrival angle ϕ_k:

$$h(t,\theta) = \sum_{k=0}^{K-1} \alpha_k \delta(t-\tau_k, \theta-\phi_k) \tag{11}$$

Accordingly, the approach to recover $h(t)$ from the frequency response $H(f)$ through the IDFT in (3) also applies to recover $h(t,\theta)$ from the conventional array frequency response $H(f,\theta)$:

$$h(t,\theta) = \sum_{l=0}^{\frac{B}{\Delta f}} H(f,\theta) e^{j2\pi ft} \tag{12}$$

The unit array impulse response centered at (τ = 0 ns, ϕ = 180°) appears in Fig. 3(a) for the conventional beamformer. The joint f and θ dependence inherent to the phase in (5) generates intractable sidelobes in $h(t,\theta)$ whose zero-crossings in turn vary jointly in the t and θ domains, precluding linear filtering techniques to suppress them.

Likewise, the frequency-invariant array impulse response $\hat{h}(t,\theta)$ can be recovered by replacing $H(f,\theta)$ in (12) instead with $\hat{H}(f,\theta)$:

$$\hat{h}(t,\theta) = \underbrace{\sum_{l=0}^{\frac{B}{\Delta f}} H(f) e^{j2\pi ft}}_{h(t)} \cdot \underbrace{\sum_{m=-\frac{P-1}{2}}^{\frac{P-1}{2}} e^{jm(\phi+\theta)}}_{\hat{h}(\theta)} \tag{13}$$

Rearranging terms above reveals that $\hat{h}(t,\theta)$ can be separated into temporal and spatial impulse responses $h(t)$ and $\hat{h}(\theta)$; moreover each is composed from a finite number of sinusoids and so viable to simple windowing techniques in suppression of the sidelobes. Figs. 3(b,c) illustrate the unit array impulse response for the frequency-invariant beamformer

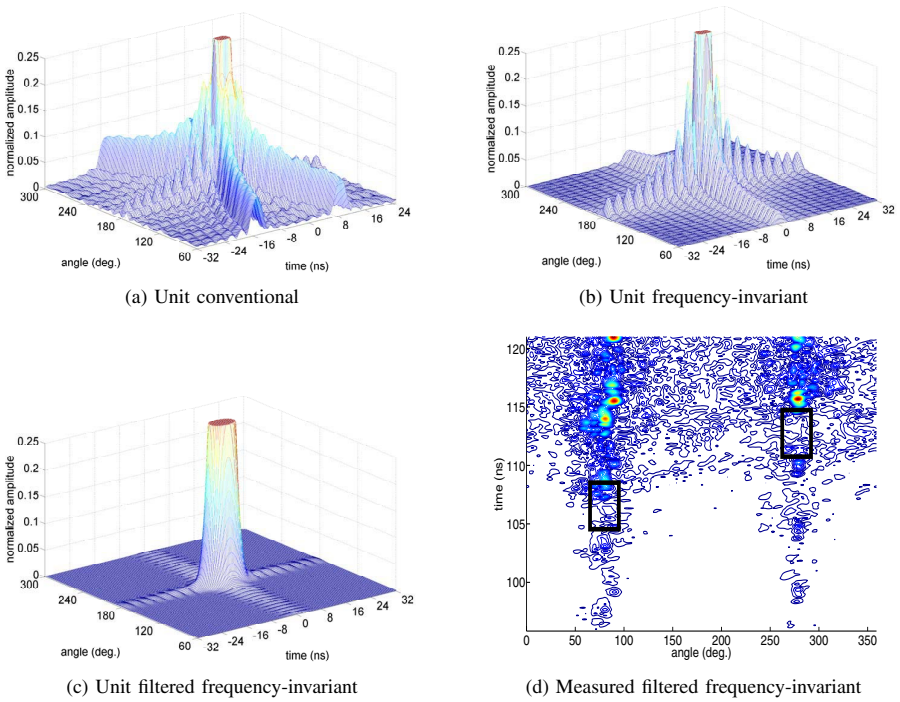

(a) Unit conventional

(b) Unit frequency-invariant

(c) Unit filtered frequency-invariant

(d) Measured filtered frequency-invariant

Fig. 3. The array impulse response.

and the filtered response using a Kaiser window in both the t and θ dimensions. While super-resolution techniques [18] show a significant improvement over the conventional IDFT techniques for smaller bandwidths, the authors in the cited work witnessed no such improvement for bandwidths in excess of 0.2 GHz, those considered in this study. Moreover such computationally intensive techniques are prohibitive when processing $P \times (\frac{B}{\Delta f} + 1)$ = 470498 points.

A. Time-of-flight and angle-of-flight estimation

The *kurtosis* measure has been recently employed in an effective thresholding technique to detect the time-of-flight from the impulse response [19]. The key strength of this measure lies in its channel invariance, enabling application of the system with no prior knowledge of the environment. In theory, it indicates the Gaussian unlikeness of a window $w[t]$ centered at t when its value defined as

$$\kappa(w[t]) = \frac{E(w^4[t])}{E^2(w^2[t])} \tag{14}$$

exceeds 3. Under the fair assumption of Gaussian noise in the channel [20], the presence of a signal is determined by computing the kurtosis of a fixed-length sliding window originating at the beginning of the impulse response; the first time sample $t = \tau_f$ in the profile at which $\kappa(w[t])$ exceeds the threshold is designated as the leading edge.

We have adapted the technique to jointly estimate the time and angle-of-flight from the array impulse response by using a two-dimensional window $w[t, \theta]$ instead. Consider a typical frequency-invariant array impulse response for a NLOS scenario in *NIST North* in Fig. 3(d). The channel delivers the arrivals in spatial clusters, an observation consistent with [6], [7]. So when searching for (τ_f, θ_f) in the two-dimensional space, we first pre-process the response to isolate a finite number of significant clusters. For each cluster q, we initiate a fixed-dimension window $w[t, \theta_q]$ at the cluster center θ_q originating at $t = 0$ and sliding only in the time dimension. Each cluster q elects a candidate leading edge as the first time sample $t = \tau_{f_q}$ in its path when $\kappa(w[t, \theta_q])$ exceeds a threshold. The first cluster is identified as the one with the smallest τ_{f_q}. The actual time and angle-of-flight are selected as the sample in the window of the first cluster with the maximum amplitude.

V. The Measurement System

Fig. 4 displays the block diagram of our measurement system. The transmitter antenna is mounted on a tripod while the uniform circular array was realized virtually by mounting the receiver antenna on a positioning table. We sweep the P elements of the array by automatically re-positioning the receiver at the successive angle θ_i around its perimeter. At each element i, the VNA in turn sweeps the discrete frequencies in the 2-8 GHz band. A total channel measurement, comprising the angle sweep and the frequency sweep at each, takes about 24 minutes. To eliminate disturbance due to the activity of personnel throughout the buildings and guarantee a static channel during the complete sweep, the measurements were conducted after working hours.

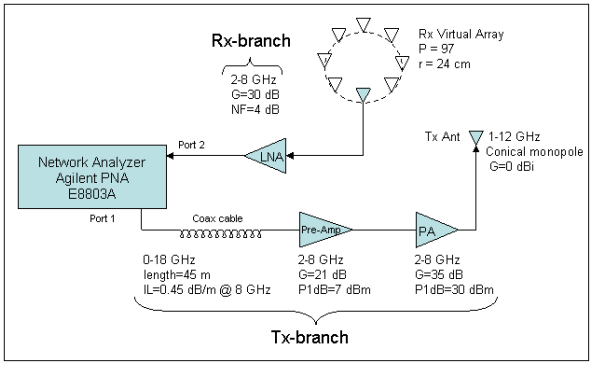

Fig. 4. Block diagram of the measurement system.

During the frequency sweep, the vector network analyzer (VNA) emits a series of tones with frequency f at Port 1 and measures the relative amplitude and phase $S_{21}(f)$ at Port 2, providing automatic phase synchronization between the two ports. The synchronization translates to a common time reference for the transmitted and received signals. The long cable enables variable positioning of the conical monopole antennas from each other throughout the test area. The preamplifier and power amplifier on the transmit branch boost the signal such that it radiates at approximately 30 dBm from the antenna. After it passes through the channel, the low-noise amplifier (LNA) on the receiver branch boosts the signal above the noise floor of Port 2 before feeding it back.

The $S_{21}(f)$-parameter of the network in Fig. 4 can be expressed as a product of the Tx-branch, the Tx-antenna, the propagation channel, the Rx-antenna, and the Rx-branch

$$\begin{aligned} S_{21}(f) &= H_{Tx}^{bra}(f) \cdot H_{Tx}^{ant}(f) \cdot H(f) \cdot H_{Rx}^{ant}(f) \cdot H_{Rx}^{bra}(f) \\ &= H_{Tx}^{bra}(f) \cdot \underbrace{H_{Tx}^{ant}(f) \cdot H_{Rx}^{ant}(f)}_{H^{ant}(f)} \cdot H(f) \cdot H_{Rx}^{bra}(f). \end{aligned} \quad (15)$$

The frequency response of the channel H is extracted by individually measuring the transmission responses $H_{Tx}^{bra}, H_{Rx}^{bra}$, and H^{ant} in advance and de-embedding them from (15). Measuring the characteristics of the antennas on a flat open field with dimensions exceeding 100 m $\times$ 100 m reduced ambient multi-path to a single ground bounce which we removed by placing electromagnetic absorbers on the ground between the antennas. We separated the antennas by a distance of 1.5 m to avoid the near-field effects and spatially averaging them through rotation with respect to each other every ten degrees. Their height was set to 1.7 m (average human height).

Note in particular the following implementation considerations:

- to account for the frequency-dependent loss in the long cable when operating across such a large bandwidth, we ramped up the emitted power at Port 1 with increasing frequency to radiate from the antenna at approximately 30 dBm across the whole band;
- we removed the LNA from the network in experiments with range below 10 m to protect it from overload and also avert its operation in the non-linear region;

TABLE I

EXPERIMENTS CONDUCTED IN MEASUREMENT CAMPAIGN.

building	wall material	LOS range (10)	NLOS range (40)
NIST North	sheet rock / aluminum studs	4.2-23.4 m	2.2-39.1 m max wall#: 9
Child Care	plaster / wooden studs	2.6-15.3 m	2.8-32.4 m max wall#: 8
Sound	cinder block	3.4-43.7 m	2.4-37.5 m max wall#: 10
Plant	steel	5.2-41.7 m	2.1-44.2 m max wall#: 10

- to extend the dynamic range of our system, we exploited the configurable test set option of the VNA to reverse the signal path in the coupler of Port 2 and bypass the 12 dB loss associated with the coupler arm. The dynamic range of the propagation channel corresponds to 140 dB as computed through [21] for an IF bandwidth of 1 kHz and a SNR of 15 dB at the receiver.

VI. THE MEASUREMENT CAMPAIGN AND RESULTS

The measurement campaign was conducted in four separate buildings on the NIST campus in Gaitherburg, Maryland, each constructed from a dominant wall material varying from sheet rock to cinder block. Table I summarizes the 40 experiments in each building (10) line-of-sight (LOS) and 40 non line-of-sight (NLOS)), including the maximum number of walls separating the transmitter and receiver.

A. Results

For each experiment in the campaign, we compute the estimated angle $\hat{\phi} = \phi_f$ and range $\hat{d} = c \cdot \tau_f$, and in turn the estimated location $\hat{\mathbf{x}} = (\hat{d}\cos\hat{\phi}, \hat{d}\sin\hat{\phi})$. The *ground-truth* angle $\bar{\phi}$, range $\bar{d}$, and location $\bar{\mathbf{x}}$ were calculated by pinpointing the coordinates of the transmitter and receiver on site with a laser tape, and subsequently finding these values using a computer-aided design (CAD) model of each building layout. The angle, range, and location errors $e_\phi = |\hat{\phi} - \bar{\phi}|$, $e_d = |\hat{d} - \bar{d}|$, and $e_{\mathbf{x}} = ||\hat{\mathbf{x}} - \bar{\mathbf{x}}||_2$ respectively serve as performance measures of the system. Table II reports the mean (μ_e), standard deviation (σ_e), minimum ($\min_e$), and maximum ($\max_e$) values of each of the three errors across the experiments associated with each cross-labeled scenario.

Fig. 5(a) illustrates the angle, range, and locations errors mutliplexed on the ordinate versus the ground-truth range for the LOS experiments in *NIST North* at (B = 6 GHz, f_c = 5 GHz). The strength of the first arrival decreases with range, but so long as it remains above the receiver sensitivity it can be detected without degrading the system performance. It follows that no obvious correlation exists between error and range in line-of-sight conditions. The angle error lies within 2°, the range error within 11 cm, and the location error within 54 cm. The LOS experiments in the other three buildings exhibit similar behavior as in *NIST North*.

The plots in Fig. 5(b-d) display the non line-of-sight scenarios in *NIST North*, *Child Care*, and *Sound* at (B = 6 GHz, f_c = 5 GHz). While notably worse than the LOS experiments, in

NIST North μ_{ϕ_e} = 3.4° (1.8% as a percentage of the maximum angle error of 180°), μ_{d_e} = 24 cm (0.6% as a percentage of the maximum ground-truth range), and $\mu_{\mathbf{x_e}}$ = 150 cm. The mean error triplet increases to (μ_{ϕ_e} = 5.5°, μ_{d_e} = 45 cm, $\mu_{\mathbf{x_e}}$ = 159 cm) in *Child Care* and (μ_{ϕ_e} = 15.2°, μ_{d_e} = 128 cm, $\mu_{\mathbf{x_e}}$ = 656 cm) in *Sound*; considering that the signal traverses up 10 walls in these two buildings, the results fare quite well. Even though UWB can successfully isolate multipath arrivals, the interaction of the signals with the walls distorts the signal: the leading-edge path propagating through walls is usually attenuated with respect to another reflected path, or even buried below the noise floor of the channel. Even if detectable, the leading edge propagates through walls slower than the speed of light, adding an irrecoverable delay with each in the estimation of τ_f since the number of walls and construction material are unknown a priori: sheet rock (cinder block) introduces an additional delay of 1.8 $\frac{\text{ns}}{\text{m wall}}$ (3.4 $\frac{\text{ns}}{\text{m wall}}$) for a total range error of 54 cm (102 cm) through 10 walls typically 10 cm thick [22]. Besides the irrecoverable delay, each interaction also deflects the leading edge off its original trajectory. These phenomena place a physical limit on the performance of the system. The system does not perform well in *Plant* (not shown), where the angle error is for the most part distributed uniformly between 0° and 35° independent of the range, and the range error lies below 500 cm only up to 15 m, clearly manifesting the impenetrable properties of metal by the direct path.

In comparing the sub-bands (B = 2 GHz, f_c = 3 GHz) and (B = 2 GHz, f_c = 3 GHz), the frequencies in the lower band penetrate the materials better [5], [23] as confirmed through the smaller mean range error in the NLOS scenarios, except in *NIST North*; the comparable errors in the latter reflect the thin sheet rock walls with favorable electromagnetic properties for which the first arrival is equally detectable in both bands even at long ranges. On the other hand, the frequencies in the upper band offer a better angular resolution (see Sec. III) and in turn yield a smaller mean angle error throughout all four buildings, except for the NLOS scenarios in *Sound*; the latter is the most challenging of the buildings in terms of wall penetration (barring of course *Plant* with impenetrable metal walls) and so for longer ranges, the system detects a stray path instead of the first, hence the larger angle error. The two opposing phenomena in the lower and upper bands yield mixed, but comparable, results in terms of mean location error across the four buildings.

VII. Conclusions

Our nominal ranging and bearing system at 6 GHz bandwidth and 5 GHz center frequency delivers a mean angle error of 1°and a mean range error of 20 cm in line-of-sight conditions up to a range of 45 m throughout all four buildings tested. The angle error increases to 3.4°, 5.5°, and 15.2° and the range error increases to 24 cm, 45 cm, and 128 cm for sheet rock, plaster, and cinder block wall materials respectively in non line-of-sight conditions; the system ranges within 35° and 500 cm up to 15 m in the steel building, but the performance degrades rapidly thereafter. In comparing sub-bands with 2 GHz bandwidth centered at 3 GHz and 7 GHz respectively, the lower band yields up to 8 cm smaller mean range error since lower frequencies penetrate walls better, but the upper band yields up to 1.2° smaller mean angle error since higher frequencies offer better angular resolution.

References

[1] C. Gentile, "Distributed Sensor Location through Linear Programming with Triangle Inequality Constraints," *IEEE Trans. on Wireless Communications*, vol. 6, no. 7, July 2007.

[2] Z. Irahhauten, H. Nikookar, and G.J.M. Janssen, "An Overview of Ultra Wide Band Indoor Channel Measurements and Modeling," *IEEE Microwave and Wireless Components Letters*, vol. 14, no. 8, Aug. 2004.

[3] J.-Y. Lee and R.A. Scholtz, "Ranging in a Dense Multipath Environment Using an UWB Radio Link," *IEEE Journal on Selected Areas in Communications*, vol. 20, no. 9, Dec. 2002.

[4] B. Denis, J. Keignart, and N. Daniele, "Impact of NLOS Propagation upon Ranging Precision in UWB Systems," *IEEE Conf. on Ultra Wideband Systems and Technologies*, Nov. 2003.

[5] C. Gentile and A. Kik, "A Comprehensive Evaluation of Indoor Ranging Using Ultra-Wideband Technology," EURASIP Journal on Wireless Communications and Networking, vol. 2007, id. 86031, 2007.

[6] R.J.-M. Cramer, R.A. Scholtz, and M.Z. Win, "Evaluation of an Ultra-Wide-Band Propagation Channel," *IEEE Trans. on Antennas and Propagation*, vol. 50, no. 5, May 2002.

[7] Q.H. Spencer, B.D. Jeffs, M.A. Jensen, and A.L. Swindlehurst, "Modeling the Statistical Time and Angle of Arrival Characteristics of an Indoor Multipath Channel," *IEEE Journal on Selected Areas in Communications*, vol. 18, no. 3, March 2000.

[8] A.S.Y. Poon and M. Ho, "Indoor Multiple-Antenna Channel Characterization from 2 to 8 GHz," *IEEE Conf. on Communications*, May 2003.

[9] S. Venkatesh, V. Bharadwaj, and R.M. Buehrer, "A New Spatial Model for Impulse-Based Ultra-Wideband Channels," *IEEE Vehicular Technology Conference, Fall*, Sept. 2005.

[10] K. Haneda, J.-I. Takada, and T. Kobayashi, "Cluster Properties Investigated From a Series of Ultrawideband Double Directional Propagation Measurements in Home Environments," *IEEE Trans. on Antennas and Propagation*, vol. 54, no. 12, Dec. 2006.

[11] H. Hashemi, "The Indoor Radio Propagation Channel," *Proceedings of the IEEE*, vol. 81, no. 7, pp. 943-968.

[12] C.A. Balanis, "Antenna Theory: Analysis and Design, Second Edition" *John Wiley & Sons, Inc.*, 1997.

[13] T.B. Vu, "Side-Lobe Control in Circular Ring Array," *IEEE Trans. on Antennas and Propagation*, vo. 41, no. 8, Aug. 1993.

[14] D.K. Cheng, "Optimization Techniques for Antenna Arrays," *Proceedings of the IEEE*, vol. 59, no. 12, Dec. 1971.

[15] N. Goto and Y. Tsunoda, "Sidelobe Reduction of Circular Arrays with a Constant Excitation Amplitude," *IEEE Trans. on Antennas and Propagation*, vol. 25, no. 6, Nov. 1977.

[16] S.C. Chan and H.H. Chen, "Uniform Concentric Circular Arrays with Frequency-Invariant Characteristics–Theory, Design, Adaptive Beamforming and DOA Estimation," *IEEE Trans. on Signal Processing*, vol. 55, no. 1, Jan. 2007.

[17] M. Wax, "Direction Finding of Coherent Signals via Spatial Smoothing for Uniform Circular Arrays," *IEEE Trans. of Antennas and Propagation*, vol. 42, no. 5, May 1994.

[18] X. Li. and K. Pahlavan, "Super-Resolution TOA Estimation With Diversity for Indoor Geolocation," *IEEE Trans. on Wireless Communications*, vol. 3, no. 1, Jan. 2004.

[19] I. Guvenc and Z. Sahinoglu, "Threshold Selection for UWB TOA Estimation Based on Kurtosis Analysis," *IEEE Communication Letters*, vol. 9, no. 12, pp. 1025-1027, Dec. 2005.

[20] I. Guvenc and Z. Sahinoglu, "Threshold-Based TOA Estimation for Impulse Radio UWB Systems," *IEEE Conf. on Ultra Wideband Systems and Technologies*, pp. 420-425, Sept. 2005.

[21] J. Keignart and N. Daniele, "Subnanosecond UWB Channel Sounding in Frequency and Temporal Domain," *IEEE Conf. on Ultra Wideband Systems and Technologies*, pp. 25-30, May 2002.

[22] A. Muqaibel, A. Safaai-Jazi, A. Bayram, A.M. Attiya, and S.M. Riad, "Ultrawideband through-the-wall propagation," *IEE Proc. on Microwaves, Antennas, and Propagation*, pp. 581-588, Dec. 2005.

[23] D. Cassioli, A. Durantini, and W. Ciccognani, "The Role of Path Loss on the Selection of the Operating Band of UWB Systems," *IEEE Conf. on Personal, Indoor and Mobile Communications*, pp. 3414-3418, June 2004.

	building	B = 6 GHz, f_c = 5 GHz			B = 2 GHz, f_c = 3 GHz			B = 2 GHz, f_c = 7 GHz		
		ϕ_e	d_e	$\mathbf{x_e}$	ϕ_e	d_e	$\mathbf{x_e}$	ϕ_e	d_e	$\mathbf{x_e}$
LOS	*NIST*	0.6, 1	9, 14	19, 26	1.3, 2.8	12, 16	44, 76	1.3, 1.3	18, 22	48, 42
	North	0, 2	2, 11	2, 54	0, 9	2, 54	2, 247	0, 4	0, 69	4, 143
	Child	1.5, 1	20, 35	38, 36	2.5, 1.2	25, 33	57, 37	1.5, 1	24, 33	39, 35
	Care	0.7, 3.1	2, 118	10, 119	0.8, 4	1, 113	14, 115	0.7, 3.1	1, 113	10, 114
	Sound	1.2, 1.3	18, 43	61, 88	1.7, 1.5	26, 37	67, 61	1.3, 0.8	23, 43	77, 69
		0.1, 4.5	1, 139	5, 277	0.1, 4.3	3, 129	6, 185	0.3, 2.6	2, 144	5, 166
	Plant	0.8, 0.8	33, 34	64, 53	1.8, 3.2	32, 32	71, 76	0.9, 0.9	30, 27	62, 66
		0.2, 2.2	3, 90	14, 161	0.2, 10.6	1, 84	13, 248	0.2, 3.2	2, 84	16, 234
NLOS	*NIST*	3.4, 2.9	24, 31	150, 194	6.7, 7.6	41, 66	284, 381	5.5, 6.1	39, 53	261, 364
	North	0.2, 14	1, 119	2, 872	0.5, 35.4	2, 320	7, 1771	0.4, 24.7	0, 245	8, 1473
	Child	5.5, 4.5	45, 36	159, 153	9.9, 7.6	47, 41	289, 291	8.4, 7.3	56, 46	247, 224
	Care	0.2, 18	4, 150	7, 779	0.1, 28.9	1, 148	24, 1263	0.3, 29.1	3, 150	7, 743
	Sound	15.2, 14.1	128, 205	656, 778	17, 16.1	169, 259	756, 965	18.8, 16.7	177, 258	830, 979
		0.4, 46.5	6, 1042	7, 2758	0.1, 61.9	10, 1322	14, 4496	0.3, 61.9	9, 1202	17, 4560
	Plant	23.2, 18.4	419, 357	995, 782	29.8, 21.2	454, 369	1111, 828	24.5, 20.2	489, 371	1143, 822
		1.2, 89.4	11, 1622	32, 2978	0.8, 85.5	5, 1617	54, 3116	0.2, 89.6	21, 1602	37, 3211

LEGEND		
ϕ_e	d_e	$\mathbf{x_e}$
μ_{ϕ_e} (deg.), σ_{ϕ_e} (deg.)	μ_{d_e} (cm), σ_{d_e} (cm)	$\mu_{\mathbf{x_e}}$ (cm), $\sigma_{\mathbf{x_e}}$ (cm)
$\min_{\phi_e}$ (deg.), $\max_{\phi_e}$ (deg.)	$\min_{d_e}$ (cm), $\max_{d_e}$ (cm)	$\min_{\mathbf{x_e}}$ (cm), $\max_{\mathbf{x_e}}$ (cm)

TABLE II

STATISTICAL RESULTS FOR EXPERIMENTS.

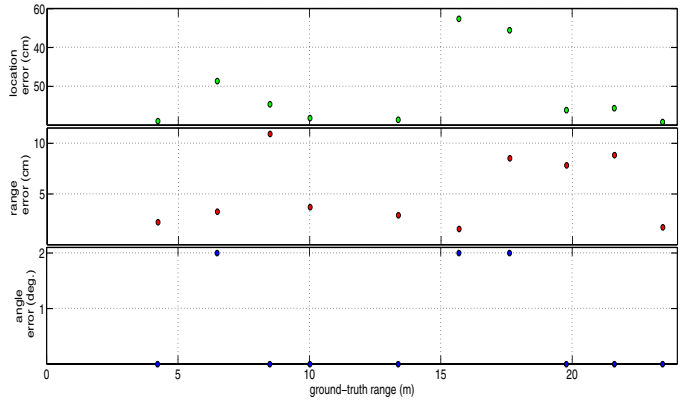

(a) *NIST North*, LOS

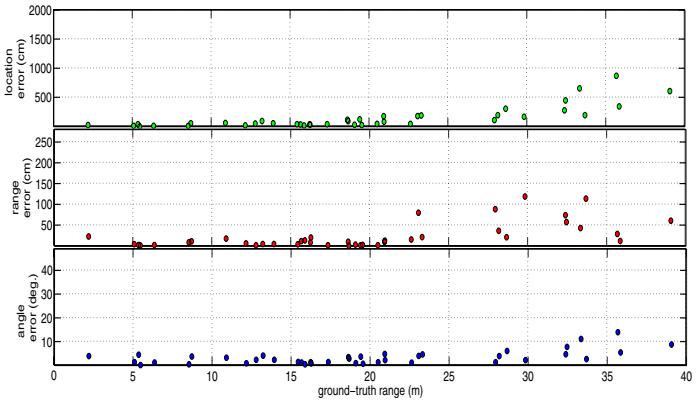

(b) *NIST North*, NLOS

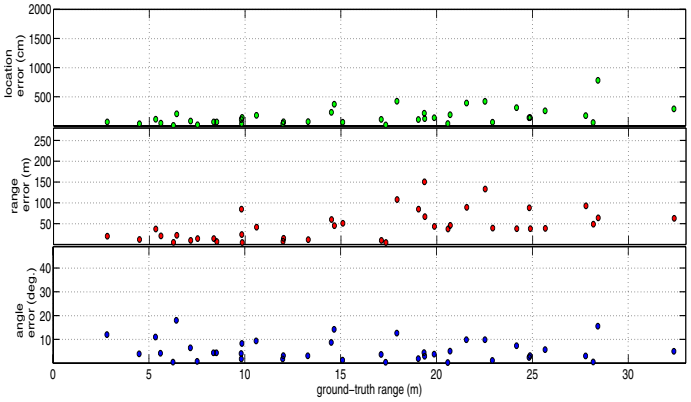

(c) *Child Care*, NLOS

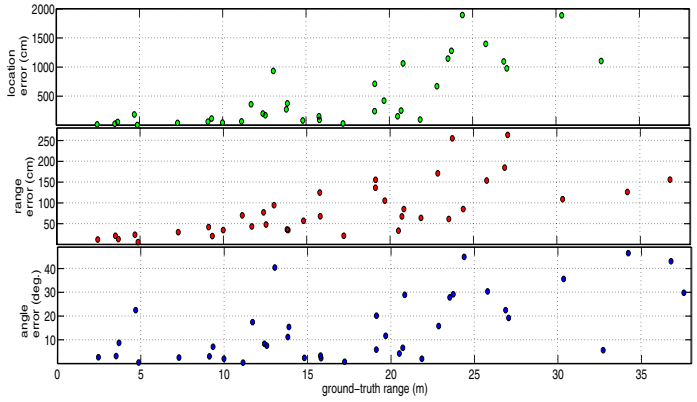

(d) *Sound*, NLOS

Fig. 5. Angle, range, and location errors versus ground-truth range for B = 6 GHz and f_c = 5 GHz.